Electronic Structure of Neodymium(III) and Europium(III) Resolved in Solution using High Resolution Optical Spectroscopy and Population Analysis

Villads M. R. Nielsen, Patrick R. Nawrocki and Thomas Just Sørensen

Department of Chemistry and Nano-Science Centre, University of Copenhagen, Universitetsparken 5, 2100 Copenhagen, Denmark. tjs@chem.ku.dk

Lanthanide luminescence; high resolution optical spectroscopy; luminescence spectroscopy; hardware; electronic structure.

Solution chemistry of the lanthanide(III) ions is unexplored and relevant: extraction and recycling processes exclusively operates in solution, MRI is a solution phase method, and bioassay are done in solution. However, the molecular structure of the lanthanide(III) ions in solution is poorly described, especially for the NIR emitting lanthanides as these are difficult to investigate using optical tools, which has limited the availability of experimental data. Here, we report on a custom built spectrometer dedicated to investigate lanthanide(III) luminescence in the NIR-region. Absorption, luminescence excitation, and luminescence spectra of five complexes of europium(III) and neodymium(III) were acquired. The obtained spectra display high spectral resolution and high

signal to noise ratios. Using the high quality data, a method for determining the electronic structure for the thermal ground states and emitting states is proposed. It combines Boltzmann distribution with population analysis and uses the experimentally determined relative transition probabilities from both excitation and emission data. The method was tested on the five europium(III) complexes, and was used to resolve the electronic structure of the ground state and the emitting state of neodymium(III) in five different solution complexes. This is the first step towards correlating optical spectra with chemical structure in solution for NIR emitting lanthanide complexes.

Introduction

The lanthanides are critical for many materials used in society. These are used in telecommunications,[1] upconverters for solar energy[2], high power lasers[3], lighting (phosphors),[4] light emitting diodes,[5] and permanent magnets.[6] The rapidly increasing consumption of the lanthanides puts pressure on improving the extraction and recycling processes.[7] While the lanthanide containing materials are solids, the preparation of the raw materials requires solution phase processes where our chemical understanding is poor.[8] To improve our understanding of the solution chemistry of these elements, new tools are required to study them in this medium. For this, optical spectroscopy offers an exciting tool that allows us to build structure-property relationships in solution.[9, 10] Studies of the lanthanide(III) ions that luminesce in the near infrared (NIR) region, such as neodymium(III), erbium(III), and ytterbium(III), is, however, still limited by low emission intensities and poor detection capabilities.[11]

Another important use of the optical properties of lanthanide(III) ions are as coordination complexes in solution. In the life science, they offer an advantageous alternative to traditional

organic chromophores as probes for bioimaging.[1, 12, 13] And in this regard, the NIR emitting probes are of particular interest for tracking and localization of biomolecules *in vivo*.[11, 14] Spectroscopy and microscopy in the NIR provides longer penetration depth, better spatial resolution, higher signal-to-noise ratios, and decreased photobleaching.[15] NIR luminescent lanthanide(III) ions such as neodymium(III), erbium(III), and ytterbium(III) are promising candidates for making molecular probes for NIR bioimaging, but for the development of probes efficient characterization is required, and today this area suffers from poor instrumentation.[16] Thus, progress in NIR emitting molecular probes is currently limited by the same challenges that oppose the field of lanthanide(III) extraction and recycling. Specifically, spectroscopic instrumentation in the NIR regions, and for the lanthanide(III) based probe, the lack of clear structure-property relationships in the f-block.[1, 17] Structure-property relationships are the direct correlation between molecular structure of the lanthanide(III) complex and the electronic structure of the $4f$ configurations. While the electronic structures of the entire series of trivalent lanthanide(III) ions have been mapped – and reported in the classical Dieke diagrams – the structural information in an optical spectrum is all found within the fine-structure originating in the crystal-field splitting, which with the right instrument can be observed in the optical spectra.[18]

The Dieke diagrams serve as a starting point when discussing energy levels of the lanthanide(III) ions, but it is only a map of the energy of multiplets of states. Each multiplet is denoted with a Russel-Saunders term symbol. In neodymium(III), each of the Russel-Saunder terms contains two or more electronic states, and the splitting of these are dictated by the crystal field. The neodymium(III) Dieke energy map was published in 1961,[19] and supported by theoretical calculations based on the intermediate coupling scheme by Wybourne in 1963.[20] The work was

continued by Crosswhite, who re-evaluated the energies and expanded the map to higher energy multiplets.[21]

The ground state crystal field splitting in neodymium(III) was mapped experimentally already in 1953 in $Nd(BrO_3)_3 \cdot 9H_2O$.[22] Other early examples where the individual Kramers doublets of the neodymium(III) ground state are resolved using optical spectroscopy include neodymium in: ethylsulfate,[23] $Y_3Al_5O_{12}$,[24] oxide crystals[25], and $YAlO_3$.[26] The level of detail is high in these single crystals systems. For single crystals, the coordination spheres and point group symmetries are readily determined by x-ray single crystal diffraction, the emission lines well ressolved due to small structural fluctuations, and the quantum yields high due to inefficient phonon relaxation pathways. These attributes are partially or completely lost in the solution.

In solution the main problems are, 1) no periodicity which limits the use of x-rays, 2) solvent interactions significantly broaden transition lines, 3) chemical equilibrium between multiple species or conformers convolute the spectra, and 4) high-energy oscillators of the solvent quench the emitting state of the lanthanide(III) ions.[10] X-ray based methods such as EXAFS[27] and total scattering methods[28] has proven to report on the solution coordination structures and coordination numbers, but lack the level of detail that x-ray techniques offer in the solid phase. The broadening observed in solution spectra is inherent and cannot be overcome at ambient temperatures. The presence of multiple different species can be assessed with spectroscopic titration series,[29] although the speciation models are seldom trivial and does not completely treat structural fluctuations.[30] And finally, the emitting states of the lanthanide(III) ions are effectively quenched by solvent molecules with high energy vibrations. This include solvent molecules or ligands that contain O-H, C-H, and N-H bonds that all act as quenchers.[13, 31] The quenching efficiency is dependent on the energy gap of the emitting states, which makes NIR emission particularly

susceptible.[32] Deuteration of the X-H oscillators is the most common method to diminish the quenching effect, but design of low-vibration ligand systems has also been explored.[33] Historically, all these factors has made it difficult to resolve optical spectra of neodymium(III).[32] The energies of the Russel-Saunders terms has been theoretically and experimentally mapped in studies by Carnall in 1965 and 1968.[34] However, neodymium(III) lifetimes in solution was not determined before 1996,[35] and the crystal field splitting in neodymium(III) has to our knowledge never been determined in solution.

To study the elusive NIR luminescence of neodymium(III), we recently built a new spectrometer that can record luminescent spectra up to 950 nm.[36] In this paper, we expand on the capabilities of the spectrometer and test the spectral quality by investigating europium(III) and neodymium(III) ions in the five different complexes shown in **Figure 1**. Two are solvates of D_2O and DMSO and three are complexes of the multi-dentate ligands DPA, EDTA, and DOTA in water. The generic electronic structures of europium(III) and neodymium(III) are included in **Figure 1**. Europium(III) is an efficient probe for molecular structure due the fact that both the $^7F_0$ ground state and the $^5D_0$ principal emitting state is characterized by just a single electronic state.[37] Thus, we use europium(III) as a reference point in our investigation of neodymium(III). Here, we start by characterizing the new capabilities of the spectrometer by describing the excitation source and discussing the necessary calibration procedures that allow us to record high quality excitation spectra. This is followed by a discussion of the spectral quality using europium(III) data, before we use a combination of peak fitting and Boltzmann analysis to resolve the crystal field splitting. Having demonstrated the capabilities of the spectrometer and the new method for resolving the crystal field splitting on europium(III), we turn to neodymium(III) and resolve the crystal field splitting of $^4F_{3/2}$ and $^4I_{9/2}$ in the five complexes.
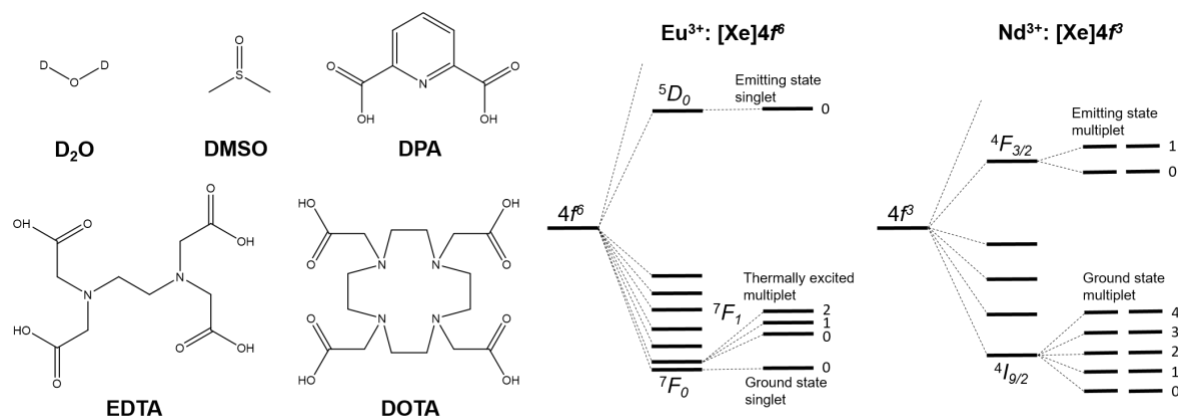
Figure 1. Left: Overview of ligand systems used to make europium(III) and neodymium(III) complexes. Right: Thermal ground and emitting multiplets of europium(III) and neodymium(III).

Methods and experimental

Chemicals

Ten samples have been made for this study. Europium(III) and neodymium(III) in the five complexes: D_2O, DMSO, DPA, EDTA, and DOTA. All chemicals were used as received.

Each sample contained 50 mM lanthanide(III); either 89.88 ± 0.2 mg $Eu(CF_3SO_3)_3$ (98 %, Strem Chemicals) or 88.72 ± 0.2 mg $Nd(CF_3SO_3)_3$ (> 97.0 %, TCI Chemicals) in the 3 mL samples.

The D_2O and DMSO samples were made by dissolving the lanthanide(III) source in 3 mL of D_2O (Eurisotop 99.90%D) and DMSO (HPLC grade, VWR), respectively.

The DOTA samples were made by dissolving 60.66 mg H_4DOTA (1,4,7,10-Tetraazacyclododecane-1,4,7,10-tetraacetic, $\geq$ 97.0 % Sigma Aldrich) in demineralized water made slightly basic using NaOH for a total volume of 3 mL.

The EDTA sample by dissolving 50.43 mg H_4EDTA (Own supply) in demineralized water made slightly basic using NaOH for a total volume of 3 mL.

The DPA samples were made by dissolving 75.20 mg H_2DPA (2,6-Pyridinedicarboxylic acid, 99 % Sigma Aldrich) in 0.8 mL 2 M NaOH until the DPA is dissolved, where 0.2 mL 2 M HCl was added. In another sample, the lanthanide(III) source is dissolved in 1 mL 2 M HCl. The lanthanide(III) solution is then added to the DPA solution for a total volume of 2 mL. Adding first 0.6 mL demineralized water and subsequently 0.4 mL 2 M HCl, the pH was adjusted to approximately pH = 4 and a total volume of 3 mL.

Optical Spectroscopy

All experiments have been done at room temperature and in 10 mm quartz cuvettes (23/Q/10) from Starna Scientific.

Absorption spectra

Absorption spectra where performed to validate excitation spectra and to verify sample purity. They were recorded on a Cary 5000 double beam absorption spectrometer from Agilent Technologies. The measurements were done in the 270 – 600 nm range for europium(III) and the 270 – 950 nm range for neodymium(III). Integration time was set to 0.2 seconds, data interval to 0.2 nm, and slit width to 0.5 nm. A lamp change is set to occur at 350 nm, a second combined detector and grating change occur at 835 nm. For each measurement, the instrument zero/baseline was determined for the empty cuvette. Absorbance spectra of the pure solvents, D_2O and DMSO were manually subtracted from the appropriate sample spectra to obtain the analysed absorbance spectra.

Emission spectra

Emission spectra where performed on our recently reported custom build spectrometer.[36] The samples where excited by a supercontinuum laser (NKT SuperK Fianium FIU-15) that was coupled to a tunable band pass filter (NKT LLTF Contrast VIS/SWIR HP8). The laser power was

set to 90% with maximum repetition rate (78MHz). A 750B grating was used for measurements below the 950 nm point, and a 1200B grating was used for measurements above 950 nm. The emission slit was set to 25 μm for all measurements. Different acquisitions settings where used for europium(III) and neodymium(III). For europium(III), the excitation wavelength was set to 465 nm, a long pass filter of 500 nm was used, and the center wavelength of the detector was set to 650 nm or 800 nm for the two regions-of-interest. For neodymium(III), the excitation wavelength was set to 580 nm, long pass filter of 800 nm was used, and the center wavelength of the detector set to 880 nm or 1050 nm for the two regions-of-interest. All acquisitions uses different exposure times and exposures per frames, the details are provided in the Supporting Information.

Excitation spectra

Excitation spectra were recorded by changing the wavelength of the excitation source through our own Python code that connects to the tunable band pass filter. At each wavelength, an emission spectrum was recorded and integrated by summing all data points spanning the region of interest—the wavelength range chosen. The step size is in all cases 0.25 nm. For europium(III), the excitation source were scanned from 450 nm to 640 nm, the exposure time per data point was 100 ms with 1 exposure per frame, and the data points were summed from 650 to 850 nm. For neodymium(III), two different acquisitions where used: 1) The excitation source were scanned from 450 to 835 nm, the exposure time was 100 ms with 1 exposure per frame, and the data points were summed from 840 to 940 nm. 2) The excitation source were scanned from 773 to 920 nm, the exposure time was 1000 ms with 10 exposures per frame, and the data points were summed from 1040 to 1070 nm.

Calibrations

Emission spectra were calibrated according to our earlier reported procedure.[36] The excitation spectra were constructed by integrating uncorrected emission data. The correction factors are linear

with respect to intensity, which yields the same relative intensities as if the excitation spectra were produced using corrected emission data. The excitation spectra were corrected for both intensity and wavelength.

Intensity correction. The true relative intensities of the excitation spectrum is convoluted by the power of the excitation source and inner filter effects of the sample. The inner filter effects are not considered in depth here, but with absorbance higher than 0.1 they cannot be disregarded.[38] The measured excitation spectrum must, however, be corrected by the flux of the excitation source at each wavelength, $J(\lambda)$.

$$I_{True}(\lambda) = \frac{I_{Measured}(\lambda)}{J(\lambda)} , J(\lambda) = \frac{P(\lambda)}{E_{photon}(\lambda)} \qquad \text{Eq. 1.}$$

Where $I_{True}(\lambda)$ is the true relative excitation intensity, $I_{Measured}(\lambda)$ is the measured excitation intensity, and $J(\lambda)$ is the photon flux of the excitation source. The photon flux is calculated from the measured power of the excitation source, $P(\lambda)$, which is corrected by the photon energy, $E_{photon}(\lambda)$. The power of the excitation source was measured with a PM16-130 power meter from Thorlabs. The measurement was done from 450 to 1000 nm with a step size of 0.25 nm and an exposure time of 10000.

Wavelength correction. The excitation system does not output the wavelength that is given as input to the software. The wavelength of the measured data must be corrected to the deviation between input and output: $\Delta(\lambda)$.

$$\lambda_{True} = \lambda_{Input} + \Delta(\lambda) \qquad \text{Eq. 2.}$$

$\Delta(\lambda)$ is obtained by measuring the laser beam scattered from a LUDOX sample in the range from 450 nm to 1000 nm. The measurement was done from 450 to 1000 nm with a step size of 1 nm, and an exposure time of 50 ms using four exposures per frame.

The laser profile was then fitted with a Gaussian function, where the center is extracted as the real wavelength used to create the calibration file.

Voigt fitting of optical transitions.

The observed optical transitions of europium(III) and neodymium(III) was fitted with Voigt functions as these were found to describe the data well. For europium(III) the excitation bands $^5D_0 \leftarrow {}^7F_0$ and $^5D_0 \leftarrow {}^7F_1$ and the emission bands $^5D_0 \rightarrow {}^7F_0$ and $^5D_0 \rightarrow {}^7F_1$ were fitted. For neodymium(III) the excitation band $^4F_{3/2} \leftarrow {}^4I_{9/2}$ and the emission band $^4F_{3/2} \rightarrow {}^4I_{9/2}$ where fitted. The fit procedure used is:

1. The number of Voigt functions used to describe each transition band was decided by visual inspection of the band. The amount of transitions that was resolved as clear peaks in the spectrum was compared to the known maximum of lines possible in each band, before a number was chosen. Note that the spectra was assumed to be from a single species, and the maximum of lines for europium(III) is four, while it is ten for neodymium(III).

2. The emission band was fitted first. In an effort to reduce fit parameters, and reduce the possibility of overfitting, the Lorentzian broadening was shared between all lines in the fits. There are thus two parameters related to the fitting of the entire system: the intensity of background and Lorentzian broadness, and there are three parameters related to each line in the bands: energy (peak position), Gaussian broadness, and integrated intensity (peak area).

3. The excitation band was fitted second. The peak center and broadness parameters of the emission peaks were transferred to the excitation peak fit. The excitation band was then fitted to the same amount of lines initially, only refining the integrated intensity. For europium(III) then the peak positions were refined. These where not refined for neodymium(III). For neodymium(III), many of the peaks where not resolved in the excitation spectra, and refining

their position would be meaningless. Further, fixing these parameters reduces the amount of fit parameters and ensures that the intensities are directly comparable under the assumption that the Stokes shift is negligible.

3b. To complement the analysis, the absorbance band was also fitted for neodymium(III). This was done using the same procedure as for the excitation band.

These three steps yield two values of interest: The energy of each transitions and the relative transition intensities.

Boltzmann analysis of spectral transitions

To extract additional information from the Voigt fit, in particular the electronic energy levels, three assumptions were made:

1. The observed optical transition intensities are measured in the steady state limit. Such that the sum of all contributions to the change of the total population of the emitting state is 0.

$$\frac{d[ES]}{dt} = -\sum_j B_{j\to i} P_j + \sum_j \gamma A_{j\leftarrow i} P_i - \sum_j O_j P_j = 0 \qquad \text{Eq. 3.}$$

Where [ES] is the excited state population, $B_{j\to i}$ the emission transition probability from j to i, P_j the thermal population of j, γ the flux of the excitation source, $A_{j\leftarrow i}$ the excitation transition probability from i to j, and O_j the relaxations from all other sources. The first two contributions are measured as the emission and excitation intensities respectively. The third contribution vanishes under normalizations in the data analysis.

2. The transition probability between two states are the same for absorption and emission.

$$B_{j\to i} = A_{j\leftarrow i} \qquad \text{Eq. 4.}$$

Where $B_{j\to i}$ and $A_{j\leftarrow i}$ are the emission transition probability and absorbance transition probability respectively.

3. The Boltzmann probability distribution describe the relative thermal populations in a system of i electronic states with energies ε_i.

$$P_i^{system} = \frac{e^{\frac{-\varepsilon_i}{k_B T}}}{\sum_i^{System} e^{\frac{-\varepsilon_i}{k_B T}}} \qquad \text{Eq. 5.}$$

Where P_i^{system} is the thermal population of state i relative to the system that is considered, ε_i is the energy of state i, $k_B T$ is the Boltzmann constant multiplied with the temperature in Kelvin.

The relative transition intensities obtained from the Voigt functions are convoluted by the relative transition probability and the thermal population of the emitting electronic state j. The relative emission transition probability from j to i is defined as the real transition probability from the state j to i divided by the sum of all transition probabilities from state j.

$$I_{j \to i}^{rel} = B_{j \to i}^{rel} P_j^{system}, \qquad B_{j \to i}^{rel} = \frac{B_{j \to i}}{\sum_i B_{j \to i}} \qquad \text{Eq. 6.}$$

Where $I_{j \to i}^{rel}$ is the observed relative emission transition intensity from j to i, $B_{j \to i}^{rel}$ the relative transition probability from j to i, P_j^{system} the relative population of state j, and $B_{j \to i}$ the absolute transition probability from j to i. The relative absorption transition intensities are normalized such that the area of all transitions is unity, and can be defined by:

$$I_{j \leftarrow i}^{rel} = A_{j \leftarrow i} P_i^{system} \qquad \text{Eq. 7.}$$

Where $I_{j \leftarrow i}^{rel}$ is the observed relative absorption transition intensity, $A_{j \leftarrow i}$ the relative transition probability from i to j, and P_i^{system} the relative population of state i.

Solving this set of equations, the thermal population of the ground state in europium(III), ^7F_J, can be calculated based on the relative intensities involving the emitting state $^5D_0$:

$$P_i^{7\text{FJ}} = N \frac{I_{0\leftarrow i}^{rel}}{B_{0\rightarrow i}^{rel}} \,, N = \left(\sum_i \frac{I_{0\leftarrow i}^{rel}}{B_{0\rightarrow i}^{rel}} \right) \qquad \text{Eq. 8.}$$

Where $P_i^{7\text{FJ}}$ is the thermal population of state i relative to the states in $^7\text{F}_\text{J}$, N is a normalizatinn constant, $I_{0\leftarrow i}^{rel}$ and $B_{0\rightarrow i}^{rel}$ are the observed relative emission transition intensity and the relative transition probability involving state 0 (in $^5\text{D}_0$) and state i (in $^7\text{F}_\text{J}$). N is introduced, as the full set of transitions in the system is not determined experimentally.

For neodymium(III), the emitting state consists of two emitting levels and this and the entire thermal ground state multiplet was described in the fits. Therefore, the true thermal populations were determined. These can be calculated from the absorption intensity into each of the emitting states. The population is therefore calculated from absorption and emission, and the displayed population was found as a weighted average:

$$P_i^{4I9/2} = \sum_j \frac{1}{\sigma_{i\leftarrow j}} \frac{I_{j\leftarrow i}^{rel}}{B_{j\rightarrow i}^{rel}} \left(\sum_j B_{j\rightarrow i}^{rel} \right) \qquad \text{Eq. 9.}$$

Where $P_i^{4I9/2}$ is the thermal population of state i relative to the states in $^4\text{I}_{9/2}$, σ_i is the error propagated fit uncertainty of each calculation, $I_{j\leftarrow i}^{rel}$ and $B_{j\rightarrow i}^{rel}$ is the observed relative emission transition intensity and the relative transition probability involving state j (in $^4\text{F}_{3/2}$) and state i (in $^4\text{F}_{9/2}$). The thermal population was thus calculated from the relative change in the emission and excitation spectra in eq. 8 and 9. The thermal population can also be calculated from the Boltzann distribution in eq. 5 when the energy and degeneracy of each involved state is known. If each fitted Voigt function only corresponds to a single electronic transition, the two populations calculated from the relative intensities and from the Boltzmann equation will give the same result. However, if the lines are from degenerate electronic states, the two calculations will not match. To evaluate deviations between the two, a Loss function was constructed:

$$L = \overset{\textit{Thermal ground state}}{\sum_{i}} \frac{(P_{obs,i} - P_{calc,i})^2}{\sigma_i^2} \qquad \text{Eq. 10.}$$

The Loss function is the weighted vector distance between the thermal populations observed in the relative intensities ($P_{obs,i}$) and the calculated Boltzmann populations ($P_{calc,i}$). The weights σ_i are the error propagated fit uncertainty of ($P_{obs,i} - P_{calc,i}$). In systems where not all states split by the crystal field according to the Russel-Saunders term descriptions, it is assumed that one or more transitions is represented by a single Voigt function in the fit of the spectra. L is calculated for all possible permutations of this assumption, and the electronic configuration with the lowest L value is assumed correct.

Results and Discussion

Calibration of Excitation data

Before the measured excitation spectra can be used, they must be corrected with respect to the excitation system. For an evaluation of the calibration procedure absorption spectra are used, as the absorbance and excitation spectra should be identical in most cases cf. the Kasha-Vavilov's rule. The calibrations follows **Equations 1 and 2**. The excitation intensity calibration function $J(\lambda)$ is shown along the wavelength calibration function $\Delta(\lambda)$ in **Figure 2**. $J(\lambda)$ is the flux of the excitation source and the excitation power is directly proportional to this value within the low absorbance limit. This can be measured directly or a fraction of the laser beam can be directed only a photodetector with a calibrated response. The power drastically falls off below 520 nm, but in the rest of the range the power is above ~1 mW. The LLTF filter changes its grating at 773 nm. This change is seen in both calibration curves.

The wavelength calibration $\Delta(\lambda)$ was obtained from fitting the data of the laser profile scattered through a sample of LUDOX to Gaussian functions. The laser scan was done from 450 to 1000

nm, and all the data is provided as Supporting Information. A qualitative assessment of the laser profiles find that two secondary peaks are observed with centers ± 2 nm from the main peak. The contribution of these is only relevant in the high energy range below 500 nm, at 500 nm they only contribute <5 %. This low energy range should be used with caution as narrow lines in the excitation spectra will be convoluted with the profile of the laser. This effect is clearly seen in the intense excitation peak at 465 nm for europium(III), see the Supporting Information. Above 500 nm the laser profile resembles a Gaussian function, and the fit of the energy profile of the laser provide two values of interest: the peak center, $\Delta(\lambda)$, and the Gaussian broadness, σ. From the determined peak center values (**Figure 2**) in the range from 450 nm to 773 nm, it can be seen that the output is1 nm below the input value. The change of grating in the LLTF at 773 nm change $\Delta(\lambda)$ to around +2 nm, with a linear decrease from +2 at 773 nm to +1 nm at 1000 nm. Furthermore, the peak center deviation is seen slightly oscillate with a period of approximately 70 nm. The Gaussian broadness in Figure 2 shows that the broadness of the laser profile drastically increases when the LLTF gratings are changed, that is the energy resolution is lower above 773 nm.

Figure 2 shows the result of doing the correction in the raw and the corrected excitation spectra of the Nd:DPA sample. The data was compared to the absorbance spectra to evaluate the quality of the calibration. Note that the sample was diluted down 5 mM, as the 50 mM sampled used for the primary instrument analysis have an absorbance above 0.1, which gives rise to non-negligible inner filter effects, see Supporting Information. We conclude that the spectral shape of the corrected excitation spectrum matches the absorbance across the entire range. From 820 nm and above the data is more noisy, due to data collection in 1060 nm band, which is beyond the operational range of the detector. An artifact is observed from 650 to 700 nm in the emission data, see the Supporting Information. This is the Raman signal from the solvent, water. This excitation

range cannot be measured using detection in the 880 nm band, and results in distortion in the spectra in **Figure 2**. These are not due artifacts in the excitation system. Finally, the data in **Figure 2** show that very noisy data is obtained below 500 nm. Based on the results shown in **Figure 2**, we conclude that the excitation system and corrections functions as intended in the range from 500 nm to 1000 nm. The range below 500 nm is limited by both laser power and laser energy profile laser, and the range above 1000 nm requires further testing and is currently limited by the detector system.
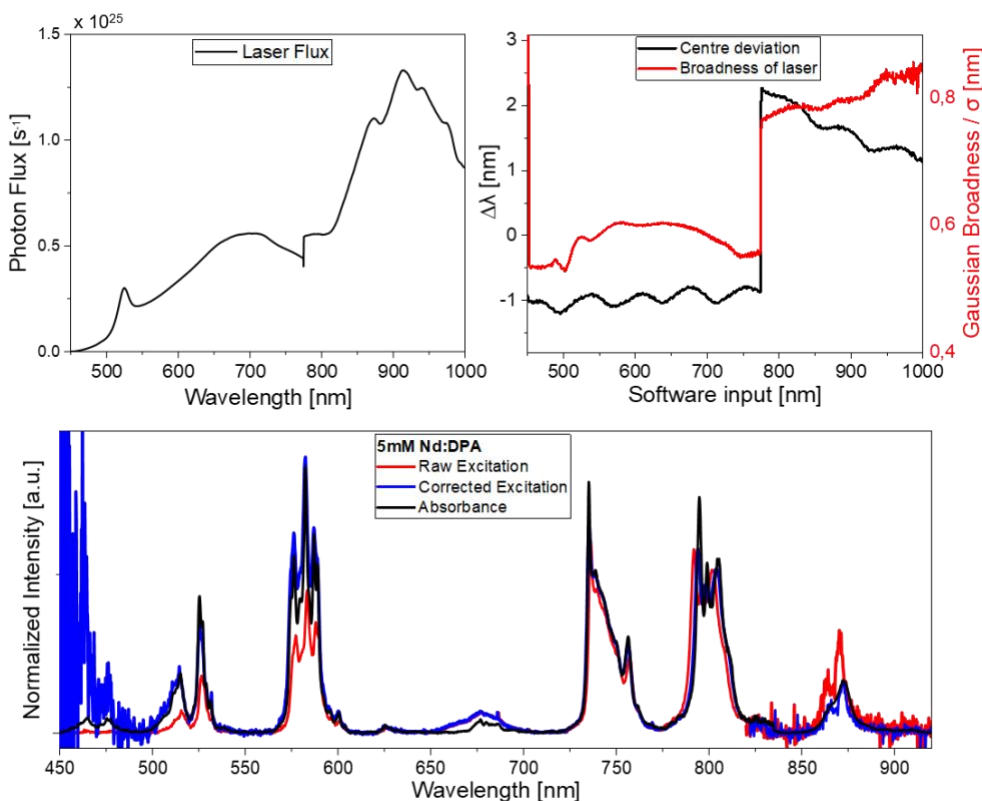
Figure 2.   Top: Photon flux of the excitation system as a function of wavelength $J(\lambda)$, and deviation between input and output wavelength of laser $\Delta(\lambda)$ shown along the peak width σ. Bottom: The raw $I_{measured}(\lambda)$ and the corrected excitation spectrum $I_{true}(\lambda)$ of a 5mM neodymium(III) Nd:DPA sample is compared to the absorbance spectrum.

VIS/NIR performance and spectra

With a calibrated excitation source and the energy resolution of the excitation spectra determined, the spectra of the ten europium(III) and neodymium(III) samples were measured.

Neodymium(III) spectra. Corrected excitation and emission spectra of the five neodymium(III) samples are shown in **Figure 3**. Raw and corrected excitation spectra are availble in the Supporting Information. The emission data are measured as two spectra with different settings: from 795 to 965 nm and from 975 to 1145 nm. The two ranges capture the $^4F_{3/2} \rightarrow \, ^4I_{9/2}$ and $^4F_{3/2} \rightarrow \, ^4I_{11/2}$ bands respectively. The quantum efficiency of the detection system is drastically lower in the second emission range, which is reflected in the lower data quality of the emission data and the excitation data integrated from this band. As the only spectrum in the set, the excitation spectrum for Nd·DOTA is not in a quality that can be used for further. Here, the absorption spectra was used instead. Finally, the $^4F_{3/2} \rightarrow \, ^4I_{13/2}$ and $^4F_{3/2} \rightarrow \, ^4I_{15/2}$ bands of neodymium(III) cannot be captured with the PyLoN detector and therefore only the two emission bands from $^4F_{3/2} \rightarrow \, ^4I_{9/2}$ and $^4F_{3/2} \rightarrow \, ^4I_{11/2}$ are shown in **Figure 3**. The overlay of the emission and excitation spectra of the $^4F_{3/2} \rightarrow \, ^4I_{9/2}$ and $^4F_{3/2} \leftarrow \, ^4I_{9/2}$ band reveal that we can resolve a similar number of lines at distinct energies, but with differences in the relative intensities due to different populations of the states in the ground and emitting multiplet. This is the basis for the analysis performed below. Note that the Stokes shift is approaching zero across the five samples. The actual Stokes shifts calculated from both emission and excitation and from emission and absorbance are compiled in Table S2 in the Supporting Information. In both calculations, the resulting Stokes shift is not considered significant assumed to be within the experimental uncertainty. The difference between the shifts calculated from the excitation data and absorbance data reveal that although there is a general bias toward a larger shift in excitation, it is within the standard deviation and cannot be assigned to the

fact that we are at the limit of the calibration. We take this as a validation of the wavelength calibration.
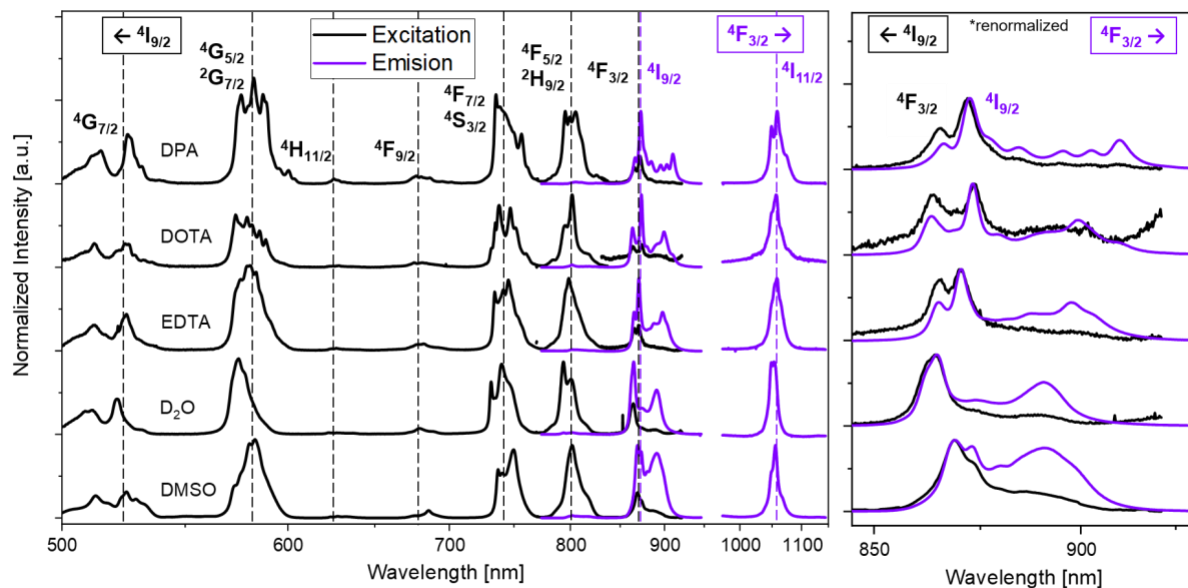

Figure 3. Excitation and emission of neodymium(III) in five different samples. Two different wavelength ranges are shown for the emission spectra. All spectra are normalized to the maximum and the relative intensities between them cannot be compared.

Europium(III) spectra. The top panel of **Figure 4** shows the excitation and absorbance spectra of the Eu·DOTA sample. Compared to neodymium(III), europium(III) has a low molar absorbance coefficient, which makes it difficult to obtain high quality absorption spectra. The high excitation power coupled with the high-sensitivity rapid acquisition spectrometer overcomes these limitations. The excitation spectra of europium(III) display a record-breaking signal-to-noise ratio and high spectral resolution in the range 500 nm and up. In this range, six excitation bands are identified in the five samples. The corrected excitation spectra of Eu·DOTA is shown in **Figure**

4, an overlay of the corrected excitation and the absorbance of the five samples are provided as Supporting Information.

The six bands observed in the excitation spectrum of the Eu·DOTA sample can be assigned to the $^5D_1 \leftarrow {}^7F_J$, and $^5D_0 \leftarrow {}^7F_J$ bands with J = 0, 1, and 2. The intensity of the transitions originating from $^7F_0$ are significantly greater than from $^7F_1$ and $^7F_2$. This is due to the higher energy terms has a smaller population at room temperature. An estimate of the mutliplet energies based on the center of the bands yield relative energies of 0, 352, and 1010 cm^{-1} for $^7F_0$, $^7F_1$, and $^7F_2$ respectively. This corresponds to a relative population of 84.4, 15.0, and 0.6 % at 293 K if the all degeneracy in the multiplets is ignored. Based on the areas of the bands one might wrongly assign the relative transition probability of $^5D_0 \leftarrow {}^7F_1$ to be ten times larger than $^5D_0 \leftarrow {}^7F_0$ cf. equation 3. To perform this analysis, the entire electronic term description must be included the 2J + 1 electronic states in each multiplet. This changes both population and transition probabilities. The populations becomes 63.8 ($^7F_0$), 34.0 ($^7F_1$), and 2.2 % ($^7F_2$) for the three terms. From these thermal weights, combined with the fact that $^5D_0 \leftarrow {}^7F_1$ contains three electronic states and three transitions, the average transition probability of $^5D_0 \leftarrow {}^7F_1$ is found to be 3.3 times larger than transition probability of the non-degenerate $^5D_0 \leftarrow {}^7F_0$ transition. These considerations are important when transition probabilities are extracted from the optical spectra.

The two inserts in the top panel of **Figure 4** show the bands originating from the 2.2 % thermally populated $^7F_2$ state magnified ten times. The bands can still be resolved, despite the low population, but they are unobservable in the absorption spectrum. **Figure 4** displays the energy levels relevant in the discussion of thermally populated states of europium(III) at 293 K. The $^7F_3$ term, at an energy of approximately 2000 cm^{-1} above the ground state, has a total population of 0.03 %. Therefore, this term, and all terms at higher energy, can be disregarded when analyzing excitation spectra.

Similarly, $^5D_1$, which is 1754 cm^{-1} higher in energy than $^5D_0$, has a thermal population of only 0.1 %. While this population is high enough for these transitions to be included and analysed, this not the aim of this study, and in the following only emission from the $^5D_0$ state is considered.

The corrected excitation and emission spectra of the five europium(III) samples are shown in the bottom panel of **Figure 4**. The corrected excitation spectra are made by integrating the total area of the emission bands in the range from 650 to 850 nm. The emission spectra of the five europium(III) samples are measured in two sets with different settings. The first setting used, was from 560 to 740 nm and captures the $^5D_0 \leftarrow$ $^7F_0$, $^7F_1$, $^7F_2$, $^7F_3$, and $^7F_4$ bands. In this range it is not an issue to capture high quality,[39, 40] and the spectra was recorded with short integration times of 0.9 s for Eu·DMSO, 0.9 s for EuDPA, 1.2 s for Eu·D$_2$O, 10 s for Eu·EDTA, and 14 s for the Eu·DOTA sample. The details on all acquisitions are available as supporting information. The second setting used, was from 730 to 880 nm and captures the $^5D_0 \leftarrow$ $^7F_5$ and $^7F_6$ bands. These are often excluded from the reported europium(III) emission spectra, due to their low intensity combined with the difficulties related to detection in the NIR range.[41] **Figure 4** include a panel where only this range is shown to demonstrate that these bands can be observed at high resolution. The integration time was increased significantly, up to several minutes to achieve this data. Note that integration time is the entire measurement time, and that this still is shorter than the measurement time on most commercial spectrometers.
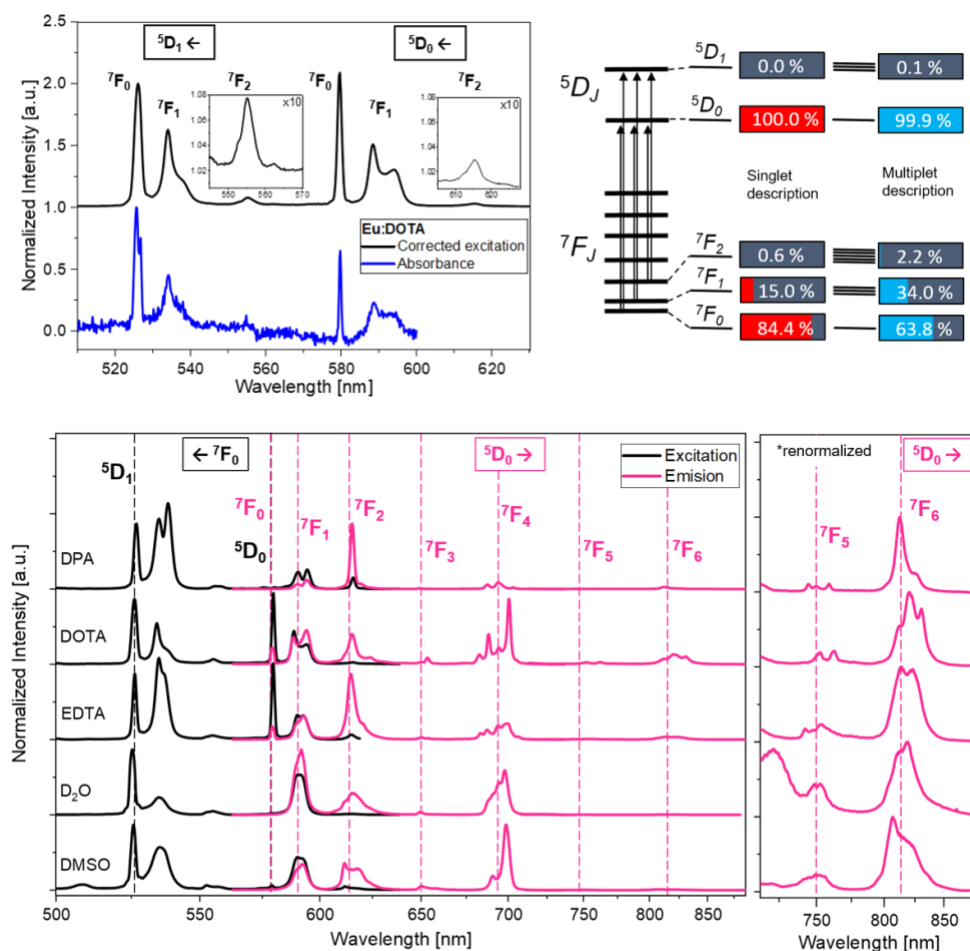
Figure 4. Top left: Corrected excitation spectrum is compared to the absorbance spectrum of Eu·DOTA. Both spectra are normalized to the maximum of the displayed wavelength range. Two inlets are provided that display a region of the excitation spectrum that has been multiplied by 10. Top right: Schematic of the electronic terms investigated and the excitation transitions visualized that was observed in spectra. Boltzmann calculations has been done for both the ^5D_J states and the ^7F_J states and the relative thermal populations are provided if a single state was present in each and if the entire multiplets are considered. Bottom: Excitation and emission spectra of europium(III) in five different systems the spectra are normalized to 1. The emission spectra in the 730 to 880 nm is shown normalized to the maximum in this region to the right.
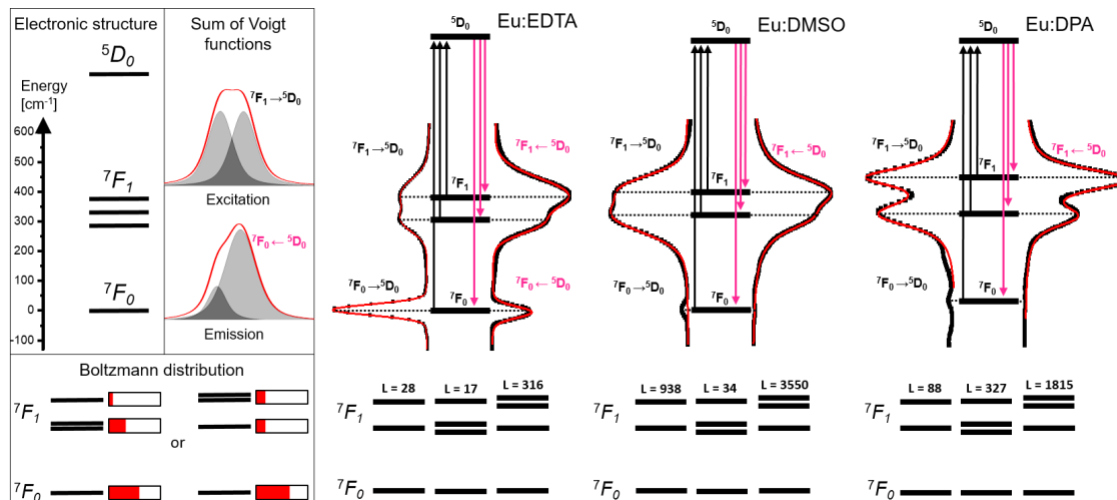
Population analyses of optical transitions

Figure 5. Left: Electronic structure of europium, Voigt fitting illustration, and plotting of the result of a Boltzmann analysis. Right: Normalised excitation (left) and emission (right) spectra of europium(III) in three different systems fitted with sum of Voigt functions. Black dots are experimental data and red lines are fits. Electronic energy levels have been aligned to the center peaks of the excitation, and the modelled electronic structures including Loss functions are shown below the spectra.

Upon closer inspection of the transitions involving $^5D_0$ and ^7F_J (J = 0 and ±1) in **Figure 5** it can be seen that the spectral shapes are similar in the emission and excitation for all samples. That is the same amount of spectral lines are observed at almost the same energies in both excitation and emission spectra. The primary difference between excitation and emission spectra from the same sample are found in the relative intensities of each line. For instance, all the high-energy lines are higher in intensity for the excitation spectra.

The lack of Stokes shift arises from the atomic nature of lanthanide(III) photophysics. The 4f-electrons are shielded by the 5s- and 5p-electrons resulting in 4f-electron configurations that only are slightly perturbed by the environment. Similarly, the crystal field is not affected by the

intraconfigurational 4f-4f transition, and the result is minimal change in molecular structure and solvation, when the central lanthanide ion is excited. Thus, the Stokes shift will approach zero, the band shape will be identical in excitation and emission, and the transition probability for the stimulated absorption that gives rise to excitation and the spontaneous emission will be identical. With these arguments, we assign the differences in relative intensities between the excitation and emission to the population of the individual states, which is described as a Boltzmann distribution.

The emission of europium(III) is dominated by the $^5D_0$ state that has a population of 99.9% at room temperature. Therefore, the relative emission intensities is equal to the relative transition probabilities. The relative intensities in the excitation spectra, however, is determined by a combination of the relative populations and the transition probabilities. To quantify the two effects, each spectra was fitted with a sum of Voigt functions. The number of functions was chosen as the number of lines that was found by cursory inspection of the each band in the spectrum. All fits are available as supporting information. **Figure 5** shows how bands are resolved by Voigt functions, and the cumulative fit of the Eu·EDTA, Eu·DMSO, and Eu·DPA spectra plotted on top of the data. Under the assumption that the absolute transition probabilities are the same in both directions, the relative populations of each state was calculated by equation 6, 7 and 8 using the relative intensities recovered in the fit. The populations were calculated from the line energies recovered in the fit using the Boltzmann equation in equation 5. **Figure 5** shows that only two lines are resolved by the fit for $^7F_1$ band for these three samples. Included in **Figure 5** is part of the electronic structure of europium(III) which shows that the $^7F_1$ band must contain three lines. That is one of the two removed lines must contain two degenerate states. As illustrated in **Figure 5** we can resolve which state is degenerate by considering the population of each energy level. If one line has an intensity larger than expected, it must arise from the degenerate state.

Consider the Eu·DMSO sample. Here, the Voigt fit recovers two lines in the $^7F_1$ band, line A and line B. The population of the corresponding energy levels has an experimentally determined population of $P_A^{7F1,rel} = 0.78 \pm 0.01$ and $P_B^{7F1,rel} = 0.20 \pm 0.01$. For a two state system, the Boltzmann distribution should be 0.619 ± 0.002 and 0.381 ± 0.002. Thus Line A must contain two states and we have resolved the spectra as line A comes from $^7F_1(+1, -1)$ and line B comes from $^7F_1(0)$. Calculating the Boltzmann population, we then get $P_{+1,-1}^{7F1,rel} = 0.765 \pm 0.002$ and $P_0^{7F1,rel} = 0.235 \pm 0.002$ much closer to the experimentally determined value. To quantify the goodness of fit of the resolved electronic states, the loss value is calculated using equitation 10. The loss function is a weighted vector distance between the experimentally observed population and the Boltzmann distribution. For the two investigated scenarios above, the loss values are $L = 938$ and $L = 34$ for the initial guess and final electronic structure, respectively. The loss function is a quantitative measure that enables a quick and robust analysis of any model. The analysis was repeated for the five europium(III) samples, and the relative transition probabilities and electronic energy levels are compiled in Table 1, below.
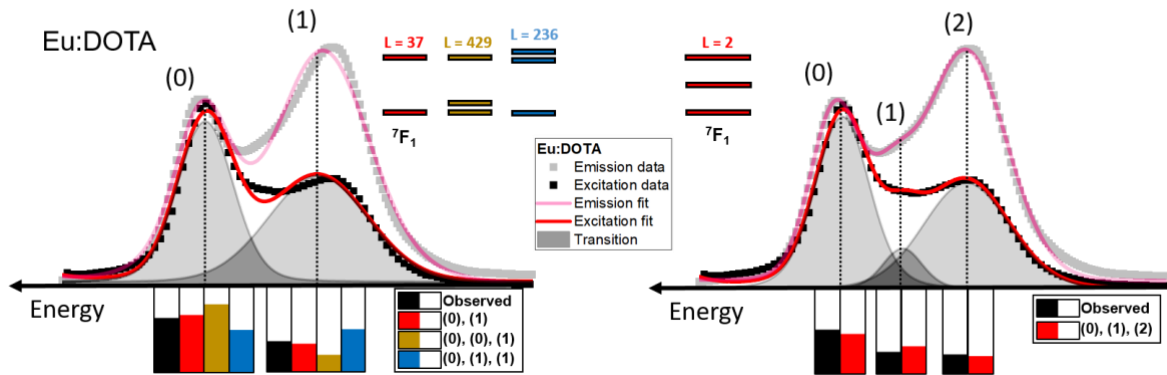

Figure 6. Lines in the $^7F_1$ band of Eu·DOTA fitted with a sum of two (left) and three (right) Voigt functions. The area of the individual excitation lines (solid, front) are displayed while the emission

areas (transparent, back) are not. The observed population is calculated and compared to the Boltzmann distribution based on the energy extracted from excitation spectra. For the fit with two lines, there are three possible electronic configurations and for the fit with three transitions, there is one possible electronic transition. The loss value has been calculated for each.

Table 1. Table of fitted relative transition probabilities and the energies of transition for europium(III) in the five different systems. The uncertainties are the fit uncertainties. If an uncertainty is not provided the values where manually extracted from the data.

Ligand	$B_{j \to i}$ [a.u.]			
	$^7F_0 \leftarrow {}^5D_0$ $m_j = 0 \leftarrow m_j = 0$	$^7F_1 \leftarrow {}^5D_0$ $(0) \leftarrow (0)$	$^7F_1 \leftarrow {}^5D_0$ $(1) \leftarrow (0)$	$^7F_1 \leftarrow {}^5D_0$ $(2) \leftarrow (0)$
DMSO	0	0.064 ± 0.001	0.127 ± 0.001	-
D2O	0	0.094 ± 0.006	0.356 ± 0.006	-
EDTA	0.020 ± 0.001	0.029 ± 0.002	0.118 ± 0.003	-
DOTA	0.017 ± 0.001	0.048 ± 0.002	0.018 ± 0.004	0.103 ± 0.002
DPA	0	0.047 ± 0.001	0.108 ± 0.001	-
Ligand	$\tilde{\upsilon}_{j \leftarrow i}$ [cm^{-1}]			
	$^7F_0 \leftarrow {}^5D_0$ $m_j = 0 \leftarrow m_j = 0$	$^7F_1 \leftarrow {}^5D_0$ $(0) \leftarrow (0)$	$^7F_1 \leftarrow {}^5D_0$ $(1) \leftarrow (0)$	$^7F_1 \leftarrow {}^5D_0$ $(2) \leftarrow (0)$
DMSO	17272	16952.7 ± 1.3	16853.6 ± 1.4	-
D2O	17278	16965.7 ± 0.5	16882.4 ± 0.5	-
EDTA	17254.2 ± 0.1	16957.7 ± 1.9	16863.2 ± 2.3	-
DOTA	17253.0 ± 0.2	16993.1 ± 1.2	16916.8 ± 3.9	16835.7 ± 3.7
DPA	17236	16945.8 ± 0.9	16821.6 ± 0.7	-

Eu·DPA and Eu·DOTA both have a large Loss value for the established electronic structure of these complexes i.e. with a degenerate $^7F_1(+1, -1)$ state higher in energy than the $^7F_1(0)$ state. Considering that $^7F_1$ band must have three states this can only be explained two ways: 1) One of the possible transitions has a transition probability approaching zero, or 2) more than one species is giving rise to the experimental data. We know this is the case for the Eu·DPA sample,[39] and in the Eu·DOTA sample we know that at least two forms of the complex is present in solution.[42] **Figure 6** shows the bands to and from the $^7F_1$ term fitted with two peaks and three peaks for Eu·DOTA. Qualitatively the three-peak fit looks much better, this however should always be the case as fitting with more peaks and thereby more free fit-parameters will give a better fit. However, combining the fit results with the Boltzmann analysis it is seen that the three-peak fit also gives a very good fit in the thermal populations with a loss value of only 2, compared to 37 for the best fit permutation in the two-peak fit. The problem is that we know this to be wrong, as the small band most likely come from the minor form of Eu·DOTA, while the two bands we wish to analyse come from the major form of Eu·DOTA. This serves as a reminder that photophysical studies must be done on samples with a known composition. When we exclude the additional band from the analysis, and enforces that there are three state in $^7F_1$ term, we can arrive at the correct electronic structure with $L = 236$ in **Figure 6**.

For neodymium(III) the excited state lifetime is much shorter, and weighted averages due to fluctuations in speciation during the excited state lifetime will be minimal[39, 42]. Thus, the population analysis was done for neodymium(III) without these consideration. The bands from the $^4F_{3/2} \rightarrow {}^4I_{9/2}$ and $^4F_{3/2} \leftarrow {}^4I_{9/2}$ transitions were observed to contain the same number of lines in both excitation/absorption and emission, and we can again assume that the differences in the spectra arise from the population of the individual energy levels. Neodymium(III) is a Kramers ion and in

the absence of an external magnetic field the $^4F_{3/2}$ can be split in two states (0) and (1), while $^4I_{9/2}$ can split in five states in a low symmetry crystal field: (0), (1), (2), (3), and (4). This is illustrated in **Figure 1**, above. For the five neodymium(III) samples the splitting of the $^4F_{3/2}$ can be directly observed, see **Figure 3**. Two strong lines are observed in all spectra, and these match the transitions between the lowest energy level of the ground state $^4I_{9/2}(0)$ and the two crystal field levels in $^4F_{3/2}$: $^4F_{3/2}(0)$ and $^4F_{3/2}(1)$. These are readily identified as the relative difference in intensity in these two transitions are the only ones affected by the population distribution in the emitting states. To illustrate the line assignment, the data from the Nd·DPA sample is shown in **Figure 7**. Here the splitting of the $^4F_{3/2}$ term is determined to be 90 cm^{-1}. Note that all the lines are doubled as transitions are observed to and from both $^4F_{3/2}(0)$ and $^4F_{3/2}(1)$. A maximum of 10 lines should be used to fit the data, but only seven lines were found in the emission spectrum by cursory inspection. After carefully assigning these seven lines in pairs with an energy separation of 90 cm^{-1}, the position of an eight line was found, and the emission and excitation data was fitted as described above. The fitted relative transition probabilities and transition energies for all samples are compiled in **Table 2** below, and the fits are available as Supporting Information. Small improvements were made as the excitation spectra of Nd·DOTA and Nd·EDTA were found to be of poor quality, the absorption spectra was used instead. And in Nd· D$_2$O, the splitting of the $^4F_{3/2}$ level is too small to resolve transitions to and from all Kramers levels in the $^4I_{9/2}$ term.

Returning to the Nd·DPA data shown in **Figure 7**, four of the five Kramers levels in of the $^4I_{9/2}$ term is resolved, and we can analyze the electronic structure based on the population of each Kramers level using equations 6, 7, and 9. By comparing the experimental population to the Boltzmann distributions using the loss function in equation 10, we can isolate the most likely electronic structure of each of the neodymium(III) complexes. The results for Nd·DPA is shown

in **Figure 7**. Five different models were tested. One with only four Kramers levels in the $^4I_{9/2}$ multiplet $^4I_{9/2}(0)(1)(2)(3)$, and all the four possible permutations $^4I_{9/2}(0,0)(1)(2)(3)$, $^4I_{9/2}(0)(1,1)(2)(3)$, $^4I_{9/2}(0)(1)(2,2)(3)$, $^4I_{9/2}(0)(1)(2)(3,3)$, where one of the Kramers levels are degenerate. As a situation with five non-degenerate Kramers levels, $^4I_{9/2}(0)(1)(2)(3)(4)$, could be excluded based on the experimental data, this was not tested.

From the Loss values, it is seen that by far the best-fit corresponds to $^4I_{9/2}(0,0)(1)(2)(3)$. It must be stressed that this does not confirm that the Kramers level is fully degenerate, but we can conclude from the observed intensity for the optical transitions to/from $^4I_{9/2}(0,0)$ dictates that there are two Kramers levels within the resolution of the experiment. Thus, we can construct the electronic structure of neodymium(III) in a DPA as five energy levels at 0, 0, 155, 295, and 478 cm^{-1}.The full analysis for all five samples and the results are available as Supporting Information.
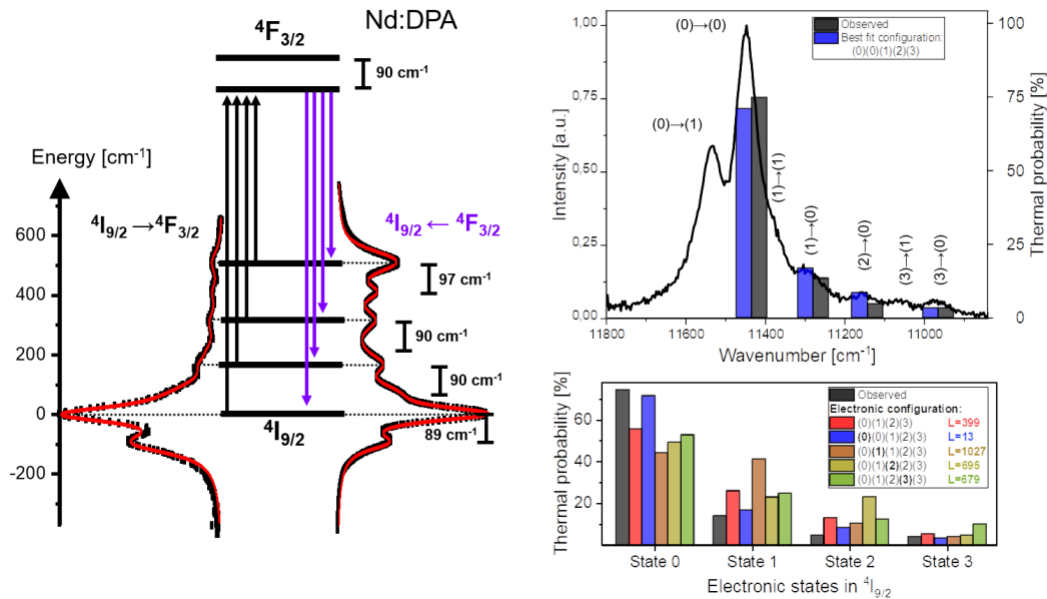

Figure 7. Left: Excitation and emission spectra of neodymium(III) in DPA fitted with sum of Voigt functions. Black dots are experimental data and the red line is the fit. The spectra are normalized to the area and are shown in the same energy range. Electronic energy levels have been

aligned to the center peaks of the excitation. Right: Nd·DPA excitation spectra overlaid with the observed thermal population and the best fit calculated Boltzmann population, and observed thermal population and the Boltzmann populations for all permutations for the electronic configurations. The loss value is shown in the legend of each configuration.

Table 2. Table of fitted relative transition probabilities and the energies of transition for neodymium(III) in the five different systems. The uncertainties are the fit uncertainties.

Ligand	$B_{j\to i}$ [a.u.] $^4F_{3/2} \to {}^4I_{9/2}$							
	(0) ← (0)	(0) ← (1)	(1) ← (0)	(1) ← (1)	(2) ← (0)	(2) ← (1)	(3) ← (0)	(3) ← (1)
DMSO	0.18 ± 0.01	0.55 ± 0.03	0.15 ± 0.05	0.32 ± 0.04	0.67 ± 0.04	0.14 ± 0.07	-	-
D2O	0.43 ± 0.01	0.26 ± 0.01	0.24 ± 0.01	-	0.41 ± 0.01	-	-	-
EDTA	0.52 ± 0.01	0.29 ± 0.01	0.30 ± 0.02	0.26 ± 0.03	0.22 ± 0.00	0.40 ± 0.01	-	-
DOTA	0.36 ± 0.02	0.47 ± 0.02	0.14 ± 0.01	0.19 ± 0.01	0.33 ± 0.02	0.31 ± 0.08	0.07 ± 0.04	0.23 ± 0.01
DPA	0.54 ± 0.09	0.24 ± 0.04	0.13 ± 0.16	0.31 ± 0.06	0.14 ± 0.04	0.11 ± 0.32	0.12 ± 0.02	0.44 ± 0.08
	$\tilde{\upsilon}_{j\leftarrow i}$ [cm⁻¹] $^4F_{3/2} \leftarrow {}^4I_{9/2}$							
Ligand	(0) ← (0)	(0) ← (1)	(1) ← (0)	(1) ← (1)	(2) ← (0)	(2) ← (1)	(3) ← (0)	(3) ← (1)
DMSO	11450.7 ± 0.3	11512.6 ± 0.3	11293.6 ± 4.7	11374.8 ± 3.9	11178.2 ± 4.6	11232.7 ± 10.0	-	-
D2O	11563.7 ± 0.6	11602.4 ± 0.9	11438.5 ± 1.0	11228.1 ± 0.5	-	11228.1 ± 0.5	-	-
EDTA	11486.3 ± 0.0	11563.4 ± 0.0	11244.8 ± 3.8	11357.6 ± 5.3	11061.5 ± 0.0	11139.8 ± 0.0	10995.5 ± 2.0	11199.6 ± 4.4
DOTA	11452.2 ± 0.1	11583.4 ± 0.3	11369.9 ± 1.4	11518.0 ± 0.8	11115.2 ± 0.6	11255.7 ± 9.1	10995.5 ± 2.0	11199.6 ± 4.4
DPA	11461.1 ± 0.1	11550.9 ± 0.4	11311.6 ± 1.5	11393.8 ± 0.6	11171.5 ± 0.7	11271.8 ± 3.6	10983.5 ± 0.3	11079.1 ± 0.6

Recovered electronic structure of europium(III) and neodymium(III)
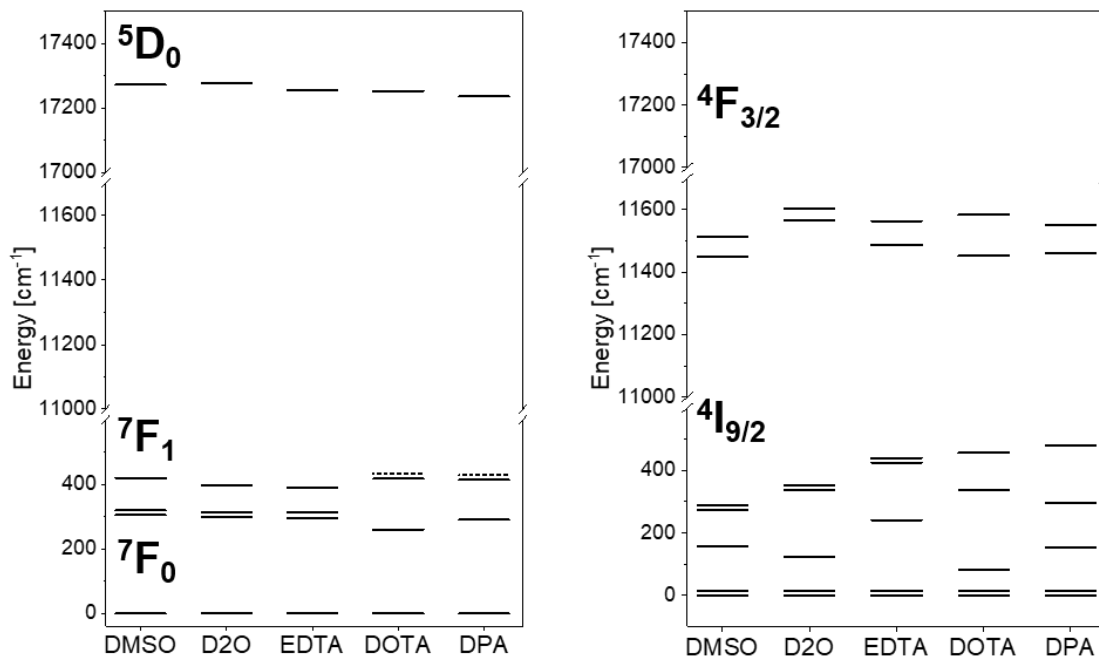

Figure 8. Room temperature electronic structure of the ground state and emitting state of europium(III) (left) and the ground multiplet and emitting multiplet of neodymium(III) (right). The levels resolved by the population analysis is shown in bold, the states known from literature are dashed.

The electronic structure of the ten samples that was resolved in the population analysis is shown in **Figure 8**. Energy levels resolved with the Boltzmann analysis is plotted 15 cm^{-1} above the fitted center energy. For neodymium(III) we report an energy splitting of the $^4I_{9/2}$ term in the range of 275 – 500 cm^{-1}, which is in the similar to what is reported in other work on solution spectra by Satten and Dieke that reported 382 cm^{-1} in Nd(BrO$_3$)3·9H$_2$O and 248 cm^{-1} in NdCl$_3$.[19, 22]

For a qualitative interpretation of the electronic structure recovered for europium(III) and neodymium(III) it can be seen that it is similar in the DMSO and D$_2$O samples. The coordination

chemistry of lanthanide(III) ions are largely dominated by non-directional and electrostatic attraction. The coordination motifs within the inner sphere of the lanthanide(III) ion can be predicted by evaluating the Thomson problem while considering the sterics of coordinating ligands.[43] Simple solvates with low denticity, such as water, experience little steric hindrance, and is found to be CN = 9 and coordinate in TTP geometry for the large lanthanide(III) ions, while the latter part of the 4f-series may be CN = 8 in a SAP geometry.[44] It is generally accepted that the simple ligand D_2O, coordinate around neodymium(III) in the TTP symmetry. DMSO is also a simple, monodentate donor molecule, which would suggest TTP symmetry, but its larger size may affect the structure. Based on the electronic structure shown in **Figure 8**, there is no indication of this for either neodymium(III) or europium(III). However, a detailed analysis of the electronic structure this is outside scope here, as it requires extensive theoretical work. What is demonstrated here is a method to resolve the electronic structure from high-resolution optical spectra.

Conclusion

The methodology needed to measure intensity and wavelength corrected excitation spectra in the range 500 to 1000 nm on our custom build spectrometer was developed and tested on ten samples. High resolution emission and excitation spectra of five europium(III) complexes and five neodymium(III) complexes. With the spectra in hand, we realized that the electronic structure of the absorbing and emitting multiplets could be determined based on the population of the individual states. A method for combining spectra deconvolution using Voigt functions, population analysis and Boltzmann distributions was developed and tested, and we conclude that it allows the electronic structure to be determined from e.g. neodymium(III) spectra recorded at room temperature in solution.

ASSOCIATED CONTENT

Supporting Information. The following files are available as supporting information.

Spectra and additional data analysis (PDF)

Python code for population analysis (PY)

AUTHOR INFORMATION

Corresponding Author

tjs@chem.ku.dk

References

(1) Bünzli, J.-C. G.; Eliseeva, S. V. Lanthanide NIR luminescence for telecommunications, bioanalyses and solar energy conversion. *Journal of Rare Earths* **2010**, *28* (6), 824-842. DOI: https://doi.org/10.1016/S1002-0721(09)60208-8.
(2) van der Ende, B. M.; Aarts, L.; Meijerink, A. Lanthanide ions as spectral converters for solar cells. *Physical Chemistry Chemical Physics* **2009**, *11* (47), 11081-11095, 10.1039/B913877C. DOI: 10.1039/B913877C. Shalav, A.; Richards, B. S.; Green, M. A. Luminescent layers for enhanced silicon solar cell performance: Up-conversion. *Solar Energy Materials and Solar Cells* **2007**, *91* (9), 829-842. DOI: https://doi.org/10.1016/j.solmat.2007.02.007.
(3) Brenier, A.; Boulon, G. Laser heated pedestal growth and spectroscopic investigations of Nd3+-doped Gd2O3 single crystal fibres. *Journal of luminescence* **1999**, *82* (4), 285-289. Gao, C.; Cui, K.; She, J.; Hou, C.; Guo, H.; Zhao, W.; Wei, W.; Peng, B. Optical properties of a novel neodymium pentafluoropropionate binuclear complex. *Inorganica Chimica Acta* **2009**, *362* (6), 2001-2005.

(4) Shinde, K. N.; Dhoble, S. J. Europium-Activated Orthophosphate Phosphors For Energy-Efficient Solid-State Lighting: A Review. *Critical Reviews in Solid State and Materials Sciences* **2014**, *39* (6), 459-479. DOI: 10.1080/10408436.2013.803456.

(5) Evans, R. C.; Douglas, P.; Winscom, C. J. Coordination complexes exhibiting room-temperature phosphorescence: Evaluation of their suitability as triplet emitters in organic light emitting diodes. *Coordination Chemistry Reviews* **2006**, *250* (15), 2093-2126. DOI: https://doi.org/10.1016/j.ccr.2006.02.007.

(6) Du, X.; Graedel, T. E. Global Rare Earth In-Use Stocks in NdFeB Permanent Magnets. *Journal of Industrial Ecology* **2011**, *15* (6), 836-843, https://doi.org/10.1111/j.1530-9290.2011.00362.x. DOI: https://doi.org/10.1111/j.1530-9290.2011.00362.x (acccessed 2022/10/06).

(7) European Commission, D.-G. f. I. M., Industry, Entrepreneurship and SMEs. COMMUNICATION FROM THE COMMISSION TO THE EUROPEAN PARLIAMENT, THE COUNCIL, THE EUROPEAN ECONOMIC AND SOCIAL COMMITTEE AND THE COMMITTEE OF THE REGIONS Critical Raw Materials Resilience: Charting a Path towards greater Security and Sustainability

2020.

(8) Yoon, H.-S.; Kim, C.-J.; Chung, K.-W.; Kim, S.-D.; Lee, J.-Y.; Kumar, J. R. Solvent extraction, separation and recovery of dysprosium (Dy) and neodymium (Nd) from aqueous solutions: Waste recycling strategies for permanent magnet processing. *Hydrometallurgy* **2016**, *165*, 27-43. DOI: https://doi.org/10.1016/j.hydromet.2016.01.028.

(9) Choppin, G. R.; Peterman, D. R. Applications of lanthanide luminescence spectroscopy to solution studies of coordination chemistry. *Coordination Chemistry Reviews* **1998**, *174* (1), 283-299. DOI: https://doi.org/10.1016/S0010-8545(98)00125-8.

(10) Yatsimirskii, K. B.; Davidenko, N. K. Absorption spectra and structure of lanthanide coordination compounds in solution. *Coordination Chemistry Reviews* **1979**, *27* (3), 223-273. DOI: https://doi.org/10.1016/S0010-8545(00)82068-8.

(11) Cao, J.; Zhu, B.; Zheng, K.; He, S.; Meng, L.; Song, J.; Yang, H. Recent Progress in NIR-II Contrast Agent for Biological Imaging. *Front Bioeng Biotechnol* **2019**, *7*, 487. DOI: 10.3389/fbioe.2019.00487 From NLM PubMed-not-MEDLINE.

(12) Bünzli, J.-C. G. Lanthanide Luminescence for Biomedical Analyses and Imaging. *Chemical Reviews* **2010**, *110* (5), 2729-2755. DOI: 10.1021/cr900362e. Uh, H.; Petoud, S. Novel antennae for the sensitization of near infrared luminescent lanthanide cations. *Comptes Rendus Chimie* **2010**, *13* (6), 668-680. DOI: https://doi.org/10.1016/j.crci.2010.05.007. Moore, E. G.; Samuel, A. P. S.; Raymond, K. N. From Antenna to Assay: Lessons Learned in Lanthanide Luminescence. *Accounts of Chemical Research* **2009**, *42* (4), 542-552. DOI: 10.1021/ar800211j.

(13) Bünzli, J.-C. G.; Piguet, C. Taking advantage of luminescent lanthanide ions. *Chemical Society Reviews* **2005**, *34* (12), 1048-1077, 10.1039/B406082M. DOI: 10.1039/B406082M.

(14) Guo, Z.; Park, S.; Yoon, J.; Shin, I. Recent progress in the development of near-infrared fluorescent probes for bioimaging applications. *Chemical Society Reviews* **2014**, *43* (1), 16-29, 10.1039/C3CS60271K. DOI: 10.1039/C3CS60271K. Yuan, L.; Lin, W.; Zheng, K.; He, L.; Huang, W. Far-red to near infrared analyte-responsive fluorescent probes based on organic fluorophore platforms for fluorescence imaging. *Chemical Society Reviews* **2013**, *42* (2), 622-661, 10.1039/C2CS35313J. DOI: 10.1039/C2CS35313J. Hilderbrand, S. A.; Weissleder, R. Near-infrared fluorescence: application to in vivo molecular imaging. *Curr Opin Chem Biol* **2010**, *14* (1), 71-79. DOI: 10.1016/j.cbpa.2009.09.029 From NLM Medline. Cai, Y.; Wei, Z.; Song, C.; Tang, C.; Han, W.; Dong, X. Optical nano-agents in the second near-infrared window for

biomedical applications. *Chemical Society Reviews* **2019**, *48* (1), 22-37, 10.1039/C8CS00494C. DOI: 10.1039/C8CS00494C. Hemmer, E.; Benayas, A.; Légaré, F.; Vetrone, F. Exploiting the biological windows: current perspectives on fluorescent bioprobes emitting above 1000 nm. *Nanoscale Horizons* **2016**, *1* (3), 168-184, 10.1039/C5NH00073D. DOI: 10.1039/C5NH00073D.

(15) Zhang, H.; Salo, D.; Kim, D. M.; Komarov, S.; Tai, Y. C.; Berezin, M. Y. Penetration depth of photons in biological tissues from hyperspectral imaging in shortwave infrared in transmission and reflection geometries. *J Biomed Opt* **2016**, *21* (12), 126006. DOI: 10.1117/1.JBO.21.12.126006 From NLM Medline.

(16) Blanco, M.; Villarroya, I. NIR spectroscopy: a rapid-response analytical tool. *TrAC Trends in Analytical Chemistry* **2002**, *21* (4), 240-250. DOI: https://doi.org/10.1016/S0165-9936(02)00404-1. Ozaki, Y. Near-Infrared Spectroscopy - Its Versatility in Analytical Chemistry. *Analytical Sciences* **2012**, *28* (6), 545-563. DOI: 10.2116/analsci.28.545.

(17) Jensen, M. P.; Bond, A. H. Comparison of covalency in the complexes of trivalent actinide and lanthanide cations. *Journal of the American Chemical Society* **2002**, *124* (33), 9870-9877.

(18) Dieke, G. H.; Crosswhite, H. M. The Spectra of the Doubly and Triply Ionized Rare Earths. *Appl. Opt.* **1963**, *2* (7), 675-686. DOI: 10.1364/AO.2.000675.

(19) Carlson, E. H.; Dieke, G. H. The State of the Nd3+ Ion as Derived from the Absorption and Fluorescence Spectra of NdCl3 and Their Zeeman Effects. *The Journal of Chemical Physics* **1961**, *34* (5), 1602-1609. DOI: 10.1063/1.1701052.

(20) Wybourne, B. G. Analysis of the Solid-State Spectra of Trivalent Neodymium and Erbium. *The Journal of Chemical Physics* **1960**, *32* (3), 639-642. DOI: 10.1063/1.1730773.

(21) Crosswhite, H. M.; Crosswhite, H.; Kaseta, F. W.; Sarup, R. The spectrum of Nd3+:LaCl3 *The Journal of Chemical Physics* **1976**, *64* (5), 1981-1985. DOI: 10.1063/1.432462.

(22) Satten, R. A. Analysis of the Spectrum of the Nd+++ Ion in the Bromate Crystal. *The Journal of Chemical Physics* **1953**, *21* (4), 637-648. DOI: 10.1063/1.1698982.

(23) Gruber, J. B.; Satten, R. A. Analysis of the Electronic Spectra of Neodymium Ethylsulfate. *The Journal of Chemical Physics* **1963**, *39* (6), 1455-1463. DOI: 10.1063/1.1734464 (acccessed 2022/10/04).

(24) Koningstein, J. A.; Geusic, J. E. Energy Levels and Crystal-Field Calculations of Neodymium in Yttrium Aluminum Garnet. *Physical Review* **1964**, *136* (3A), A711-A716. DOI: 10.1103/PhysRev.136.A711.

(25) Henderson, J. R.; Muramoto, M.; Gruber, J. B. Spectrum of Nd3+ in Lanthanide Oxide Crystals. *The Journal of Chemical Physics* **1967**, *46* (7), 2515-2520. DOI: 10.1063/1.1841079 (acccessed 2022/10/04).

(26) Weber, M. J.; Varitimos, T. E. Optical Spectra and Intensities of Nd3+ in YAlO3. *Journal of Applied Physics* **1971**, *42* (12), 4996-5005. DOI: 10.1063/1.1659885 (acccessed 2022/10/04).

(27) Persson, I.; D'Angelo, P.; De Panfilis, S.; Sandström, M.; Eriksson, L. Hydration of Lanthanoid(III) Ions in Aqueous Solution and Crystalline Hydrates Studied by EXAFS Spectroscopy and Crystallography: The Myth of the "Gadolinium Break". *Chemistry – A European Journal* **2008**, *14* (10), 3056-3066, https://doi.org/10.1002/chem.200701281. DOI: https://doi.org/10.1002/chem.200701281 (acccessed 2022/10/07). Nockemann, P.; Thijs, B.; Lunstroot, K.; Parac-Vogt, T. N.; Görller-Walrand, C.; Binnemans, K.; Van Hecke, K.; Van Meervelt, L.; Nikitenko, S.; Daniels, J.; et al. Speciation of Rare-Earth Metal Complexes in Ionic Liquids: A Multiple-Technique Approach. *Chemistry – A European Journal* **2009**, *15* (6), 1449-1461, https://doi.org/10.1002/chem.200801418. DOI: https://doi.org/10.1002/chem.200801418 (acccessed 2022/10/07).

(28) Kofod, N.; Nawrocki, P.; Juelsholt, M.; Christiansen, T. L.; Jensen, K. M. Ø.; Sørensen, T. J. Solution Structure, Electronic Energy Levels, and Photophysical Properties of [Eu(MeOH)n-2 m(NO3)m]3- m+Complexes. *Inorganic Chemistry* **2020**, *59* (15), 10409-10421. DOI: 10.1021/acs.inorgchem.0c00056.

(29) Nawrocki, P. R.; Kofod, N.; Juelsholt, M.; Jensen, K. M. Ø.; Sørensen, T. J. The effect of weighted averages when determining the speciation and structure–property relationships of europium(iii) dipicolinate complexes. *Physical Chemistry Chemical Physics* **2020**, *22* (22), 12794-12805, 10.1039/D0CP00989J. DOI: 10.1039/D0CP00989J. Maupin, C. L.; Smith, K. C.; Riehl, J. P. Quantitative determination of Eu(III) complex speciation in aqueous complexes of Eu(III) with oxydiacetic acid using 5D0 → 7F0 excitation spectroscopy. *Journal of Alloys and Compounds* **1997**, *249* (1), 181-184. DOI: https://doi.org/10.1016/S0925-8388(96)02531-5.

(30) Nielsen, L. G.; Sørensen, T. J. Including and Declaring Structural Fluctuations in the Study of Lanthanide(III) Coordination Chemistry in Solution. *Inorganic Chemistry* **2019**, (Iii). DOI: 10.1021/acs.inorgchem.9b01571.

(31) Haas, Y.; Stein, G. Pathways of radiative and radiationless transitions in europium(III) solutions. The role of high energy vibrations. *The Journal of Physical Chemistry* **1971**, *75* (24), 3677-3681. DOI: 10.1021/j100693a006. Døssing, A. Luminescence from Lanthanide(3+) Ions in Solution. *European Journal of Inorganic Chemistry* **2005**, *2005* (8), 1425-1434, https://doi.org/10.1002/ejic.200401043. DOI: https://doi.org/10.1002/ejic.200401043 (acccessed 2022/10/04). Comby, S.; Bünzli, J.-C. G. Chapter 235 Lanthanide Near-Infrared Luminescence in Molecular Probes and Devices. In *Handbook on the Physics and Chemistry of Rare Earths*, Gschneidner, K. A., Bünzli, J.-C., Pecharsky, V. K. Eds.; Vol. 37; Elsevier, 2007; pp 217-470.

(32) Stein, G.; Würzberg, E. Energy gap law in the solvent isotope effect on radiationless transitions of rare earth ions. *The Journal of Chemical Physics* **1975**, *62* (1), 208-213. DOI: 10.1063/1.430264 (acccessed 2022/10/04).

(33) Kropp, J. L.; Windsor, M. W. Luminescence and Energy Transfer in Solutions of Rare-Earth Complexes. I. Enhancement of Fluorescence by Deuterium Substitution. *The Journal of Chemical Physics* **1965**, *42* (5), 1599-1608. DOI: 10.1063/1.1696166 (acccessed 2022/10/04). Yanagida, S.; Hasegawa, Y.; Murakoshi, K.; Wada, Y.; Nakashima, N.; Yamanaka, T. Strategies for enhancing photoluminescence of Nd3+ in liquid media. *Coordination Chemistry Reviews* **1998**, *171*, 461-480. DOI: https://doi.org/10.1016/S0010-8545(98)90069-8. Bünzli, J.-C. G. On the design of highly luminescent lanthanide complexes. *Coordination Chemistry Reviews* **2015**, *293-294*, 19-47. DOI: https://doi.org/10.1016/j.ccr.2014.10.013. Hu, J.-Y.; Ning, Y.; Meng, Y.-S.; Zhang, J.; Wu, Z.-Y.; Gao, S.; Zhang, J.-L. Highly near-IR emissive ytterbium(iii) complexes with unprecedented quantum yields. *Chemical Science* **2017**, *8* (4), 2702-2709, 10.1039/C6SC05021B. DOI: 10.1039/C6SC05021B.

(34) Carnall, W. T.; Fields, P. R.; Wybourne, B. G. Spectral Intensities of the Trivalent Lanthanides and Actinides in Solution. I. Pr3+, Nd3+, Er3+, Tm3+, and Yb3+. *The Journal of Chemical Physics* **1965**, *42* (11), 3797-3806. DOI: 10.1063/1.1695840. Carnall, W. T.; Fields, P. R.; Rajnak, K. Electronic Energy Levels in the Trivalent Lanthanide Aquo Ions. I. Pr3+, Nd3+, Pm3+, Sm3+, Dy3+, Ho3+, Er3+, and Tm3+. *The Journal of Chemical Physics* **1968**, *49* (10), 4424-4442. DOI: 10.1063/1.1669893.

(35) Beeby, A.; Faulkner, S. Luminescence from neodymium(III) in solution. *Chemical Physics Letters* **1997**, *266* (1), 116-122. DOI: https://doi.org/10.1016/S0009-2614(96)01520-5.

(36) Nawrocki, P. R.; Nielsen, V. M. R.; Sørensen, T. J. A high-sensitivity rapid acquisition spectrometer for lanthanide(III) luminescence. *Methods and Applications in Fluorescence* **2022**.

(37) Binnemans, K. Interpretation of europium(III) spectra. *Coordination Chemistry Reviews* **2015**, *295*, 1-45. DOI: 10.1016/j.ccr.2015.02.015. Tanner, P. A. Some misconceptions concerning the electronic spectra of tri-positive europium and cerium. *Chemical Society Reviews* **2013**, *42* (12), 5090-5101. DOI: 10.1039/c3cs60033e. Werts, M. H. V.; Jukes, R. T. F.; Verhoeven, J. W. The emission spectrum and the radiative lifetime of Eu3+ in luminescent lanthanide complexes. *Physical Chemistry Chemical Physics* **2002**, *4* (9), 1542-1548. DOI: 10.1039/b107770h.

(38) Kimball, J.; Chavez, J.; Ceresa, L.; Kitchner, E.; Nurekeyev, Z.; Doan, H.; Szabelski, M.; Borejdo, J.; Gryczynski, I.; Gryczynski, Z. On the origin and correction for inner filter effects in fluorescence Part I: primary inner filter effect-the proper approach for sample absorbance correction. *Methods and Applications in Fluorescence* **2020**, *8* (3), 033002. DOI: 10.1088/2050-6120/ab947c. Ceresa, L.; Kimball, J.; Chavez, J.; Kitchner, E.; Nurekeyev, Z.; Doan, H.; Borejdo, J.; Gryczynski, I.; Gryczynski, Z. On the origin and correction for inner filter effects in fluorescence. Part II: secondary inner filter effect -the proper use of front-face configuration for highly absorbing and scattering samples. *Methods and Applications in Fluorescence* **2021**, *9* (3), 035005. DOI: 10.1088/2050-6120/ac0243.

(39) Nawrocki, P. R.; Jensen, K. M. Ø.; Sørensen, T. J. The effect of weighted averages when determining the speciation and structure–property relationships of europium (iii) dipicolinate complexes. *PCCP* **2020**, *22* (22), 12794-12805.

(40) Kofod, N.; Nawrocki, P.; Juelsholt, M.; Christiansen, T. L.; Jensen, K. M. Ø.; Sørensen, T. J. Solution Structure, Electronic Energy Levels, and Photophysical Properties of [Eu(MeOH)n−2m(NO3)m]3–m+ Complexes. *Inorganic chemistry* **2020**, *59* (15), 10409-10421. DOI: 10.1021/acs.inorgchem.0c00056.

(41) Nawrocki, P. R.; Nielsen, V. M.; Sørensen, T. J. A high-sensitivity rapid acquisition spectrometer for lanthanide (III) luminescence. *Methods and Applications in Fluorescence* **2022**. Moret, E.; Bünzli, J.-C. G.; Schenk, K. J. Structural and luminescence study of europium and terbium nitrate hexahydrates. *Inorganica Chimica Acta* **1990**, *178* (1), 83-88. DOI: https://doi.org/10.1016/S0020-1693(00)88138-4.

(42) Nielsen, L. G.; Sørensen, T. J. Including and Declaring Structural Fluctuations in the Study of Lanthanide(III) Coordination Chemistry in Solution. *Inorganic Chemistry* **2020**, *59* (1), 94-105. DOI: 10.1021/acs.inorgchem.9b01571.

(43) Thomson, J. J. XXIV. On the structure of the atom: an investigation of the stability and periods of oscillation of a number of corpuscles arranged at equal intervals around the circumference of a circle; with application of the results to the theory of atomic structure. *The London, Edinburgh, and Dublin Philosophical Magazine and Journal of Science* **1904**, *7* (39), 237-265. DOI: 10.1080/14786440409463107. Drew, M. G. B. Structures of high coordination complexes. *Coordin Chem Rev* **1977**, *24* (2), 179-275. DOI: https://doi.org/10.1016/S0010-8545(00)80338-0.

(44) Helm, L.; Merbach, A. E. Inorganic and bioinorganic solvent exchange mechanisms. *Chemical reviews* **2005**, *105* (6), 1923-1960. Kofod, N.; Nawrocki, P.; Platas-Iglesias, C.; Sørensen, T. J. Electronic Structure of Ytterbium (III) Solvates—a Combined Spectroscopic and Theoretical Study. *Inorganic Chemistry* **2021**.